RESEARCH ARTICLE

NANO · MICRO small
www.small-journal.com

Direct Laser Writing of Silica Nanoparticle Nanocomposites: Probing Mechanical Reinforcement and Understanding Structural Color from Design Parameters

Amrutha Augustine, Jing Qian, Teodora Faraone, Srikanth Kolagatla, Nadezda Prochukhan, Michael A. Morris, A. Louise Bradley, Larisa Florea,* and Colm Delaney**

Nanocomposite materials have been thoroughly exploited in additive manufacturing, as a means to alter physical, chemical, and optical properties of resulting structures. Herein, nanocomposite materials suitable for direct laser writing (DLW) by two-photon polymerization are presented. These materials, comprising silica nanoparticles, bring significant added value to the technology through physical reinforcement and controllable photonic properties. Incorporation into acrylate photoresists, via a one-step fabrication process, enables the formation of complex structures with large overhangs. The inclusion of 150 nm silica nanoparticles in DLW photoresists at high concentrations, allows for the fabrication of composite microstructures that show reflected color, a product of the relative contributions from the quasi-ordering and random scattering. Using common DLW design parameters, such as slicing distance and structure dimension, a wide gamut of structural color, in solution, using a set concentration of nanoparticles is demonstrated. Numerical modeling is employed to predict the reflected wavelength of the pixel arrays, across the visible spectrum, and this information is used to encode reflected colors into different pixel arrays.

1. Introduction

Direct laser writing by two-photon polymerization (DLW-2PP) is a maskless optical lithographic technique that enables the fabrication of complex 3D microstructures with sub 300 nm resolution and minimal topological constraints.[1,2] Typically, 2PP is induced by the absorption of two near-infrared (NIR) photons by an initiator molecule in a photosensitive resin. This polymerization is confined at the focal volume and 3D structures are fabricated by moving the focal point in the resin along the designed path. The desire to create 3D micro and nanostructures has been of great interest in the fields of microelectromechanical systems (MEMS),[3] micro/nanofluidics,[4] photonics,[5] electronics and bioelectronics,[6] microrobotics,[7] and tissue engineering,[8] among others.

The addition of nanofillers to photoresists has been demonstrated to bring added functionality to polymer microstructures produced via DLW, such as enhanced mechanical,[9] conductive,[10] magnetic,[11] piezoelectric,[12] and optical properties.[13] Groetsch et al.[14] reported the reinforcement of microstructures produced via 2PP in a methacrylate-based photoresist through the addition of 4.5 wt% of cellulose nanocrystals (CNCs), leading to a 70% increase in yield stress, 88% increase in compressive strength and a 100% increase in Young's modulus compared to the neat photoresist. Using a similar approach, Xiong et al.[9] demonstrated a significant improvement in the electrical and mechanical properties of an acrylate thiol-based photoresist through the incorporation of multi-walled carbon nanotubes (MW-CNT). Conductivities of 7.54 and 46.8 S m^{-1} were obtained by dispersing MW-CNTs at 0.15 and 0.2 wt% concentrations, respectively, in the insulating polymer, along with an increase in Young's modulus and material hardness. Dadras-Toussi et al.[15] fabricated 3D organic semiconductor (OS) composite microstructures where enhanced electrical conductivity of the polymer by 10 orders of magnitude was observed with an inclusion of 0.5 wt% OS material. These composite microstructures

A. Augustine, T. Faraone, S. Kolagatla, N. Prochukhan, M. A. Morris, L. Florea, C. Delaney
School of Chemistry & AMBER
The SFI Research Centre for Advanced Materials and BioEngineering Research
Trinity College Dublin
Dublin D02PN40, Ireland
E-mail: floreal@tcd.ie; cdelane5@tcd.ie

J. Qian, A. L. Bradley
School of Physics and AMBER
The SFI Research Centre for Advanced Materials and BioEngineering Research
Trinity College Dublin
Dublin D02PN40, Ireland
E-mail: bradlel@tcd.ie

The ORCID identification number(s) for the author(s) of this article can be found under https://doi.org/10.1002/smll.202310058

DOI: 10.1002/smll.202310058

were further shown to be biocompatible and demonstrated as glucose biosensors upon encapsulation of glucose oxidase.[15] Marino et al.[12] reported the use of 2PP to fabricate structures suitable for cell culturing using a piezoelectric nanocomposite resist. The resist was composed of commercially available Ormocomp doped with 10 wt% piezoelectric barium titanate nanoparticles (BTNPs). Nanocomposite materials have also been shown to be useful for the modulation of the optical properties of polymer microstructures fabricated by 2PP. Gua et al.[16] reported the tuning of the effective refractive index by the addition of varying concentrations of TiO_2 NPs in Ormocer b59, resulting in a change of the refractive index from 1.554 to ≈1.569 as the concentration of TiO_2 was increased from 0 to 3.25 wt%.

The inclusion of nanofillers can also result in desired optical properties in composite materials through structural coloration. The generation of structural color results from the interaction of light with micro- or nano-structures, where an ordered arrangement of these structures at the nanometer scale often plays a substantial role.[17,18] Several examples of 3D nanocomposite structures showing structural color have been reported at both macro and micro-scales. Liao et al.[19] developed a non-close-packed colloidal photonic crystal (NCPC) ink composed of highly charged elastic nanoparticles (HENPs). Digital light processing (DLP) based 3D printing of this NCPC ink, which contained the thermo-responsive polymer poly(*N*-isopropylacrylamide) (PNIPAM) along with the HENPs, enabled the fabrication of structures with temperature-responsive structural colors and shapes, and multicolor patterns featuring tunable structural colors. Hou et al.[20] fabricated a photonic crystal (PC) microchip by inkjet printing, which allowed highly sensitive ultra-trace detection of fluorescence analytes and fluorophore-based assays. The microchip was composed of a hydrophobic polydimethylsiloxane (PDMS) substrate containing PC dots composed of assembled hydrophilic monodispersed poly(styrene-methyl methacrylate-acrylic acid) spheres. Wei et al.[21] synthesized a multifunctional nanocomposite ink composed of carbon nanotubes (CNT) and cellulose nanofibers (CNF) dispersed into hydroxypropyl cellulose (HPC) aqueous solution. The HPC-CNT-CNF components were self-assembled to form dynamic cholesteric liquid crystal nanostructures. HPC-CNT-CNF composites were 3D printed via direct ink writing to fabricate an optical and resistive strain sensor.

Fabrication of structures containing silica (SiO_2) nanoparticles (NPs) has been of great interest for the generation of nanocomposite structures for photonic applications. Bai et al.[22] reported the synthesis of vapor-responsive colloidal photonic crystal patterns by inkjet printing of mesoporous silica nanoparticle (MSN) ink with reversible color-shifting properties controlled by the design of the MSNs. Lai et al.[23] fabricated quasi-amorphous composite films made via UV polymerization of an ethoxylated trimethylolpropane triacrylate SiO_2 NP dispersion. Uniform structural colors spanning from the UV to the IR regions were observed and confirmed to originate from constructive interference of light from the short-range ordered quasi-amorphous structures. These resin films were demonstrated for application as novel optical filters for white light-emitting diodes. Along with photonic properties, SiO_2 NPs have also been applied in mechanical reinforcement. Arjmandi et al.[24] studied the improvements in mechanical properties such as the compressive modulus and elastic modulus of an interpenetrating polymer network of alginate-polyacrylamide (ALG-PAAm) in which SiO_2 NPs were added. The resultant hydrogel showed an increase in the elastic modulus of 38.6% with the incorporation of 4% concentration of SiO_2 NPs. This can be attributed to effective stress transfer between the polymer matrix and SiO_2 NPs.[25] Additionally, Luo et al.[26] reported an improvement in the tensile strength and Young's modulus of polyurethane films by ≈41% and 47%, respectively, through the incorporation of 1.5 wt% of SiO_2 NPs.

To date, the development of two-photon polymerizable silica nanocomposite photoresists has followed two distinct routes. The first motivation for investigating this was the generation of 3D printed highly transparent glasses. This approach requires the dispersion of silica nanoparticles at a high volume percentage in viscous photoresists containing multiarm acrylate crosslinkers. As in bulk glass synthesis, this requires a high-temperature de-binding step, followed by sintering at >1000 °C. In 2021, this was achieved by Doualle et al.[27] on the macro scale using hydrophilic fumed silica nanoparticles with a hydroxyl-ethyl-methacrylate monomer. Similarly, Kotz et al.[28] used a prototype resin from Nanoscribe Gmbh to create optical elements on the micron-to-millimeter scale. Using PEG-functionalized colloidal silica nanoparticles, Wen et al.[29] optimized the printing process to achieve resolution below 200 nm, with different polymorphs controlled by sintering processes. The printed SiO_2 structures permitted doping and co-doping with rare-earth salts showing strong photoluminescence at desired wavelengths. In all these cases, DLW was used as a means of fabricating dispersions of silica nanoparticles into 3D structures for subsequent de-binding and sintering. In 2022, Liu et al.[17] developed the first means of achieving an ordered arrangement of SiO_2 nanoparticles in different soft polymer matrices. This was made possible through the use of a sacrificial scaffold-mediated two-photon lithography strategy using a degradable disulfide monomer. After degradation in tris-(2-carboxyethyl) phosphine (1 h) and infiltration with the new monomeric cocktail (24 h), using a 25× objective, a range of macroscopic structures with micron feature sizes were fabricated. Variation of polychromatic structural colors was achieved through manipulation of the exposure dose of the laser. In this work, we report that methods of controlling structural coloration are not only limited to laser power (LP) and type of precursor, but can also be varied by changing parameters such as NP concentration, slicing distance, and structural dimensions of the microstructures.

Herein, we present an apt amalgamation of top–down and bottom–up fabrication strategies by creating photonic microstructures using DLW via 2PP. SiO_2 NPs of varying sizes were synthesized via the Stöber process and successfully incorporated into acrylate-based photoresists at varying concentrations, to form stable dispersions. After the successful fabrication of stable microstructures, the ability of SiO_2 NPs to enhance the mechanical properties of the microstructures was investigated. Furthermore, above a threshold volume fraction of SiO_2 NPs, the repulsive interparticle forces promote self-assembly. Photopolymerization of this nanoparticle photoresist via 2PP allows for the realization of photonic microstructures responsive to changes in immersion solvent due to varying interparticle spacing. Moreover,

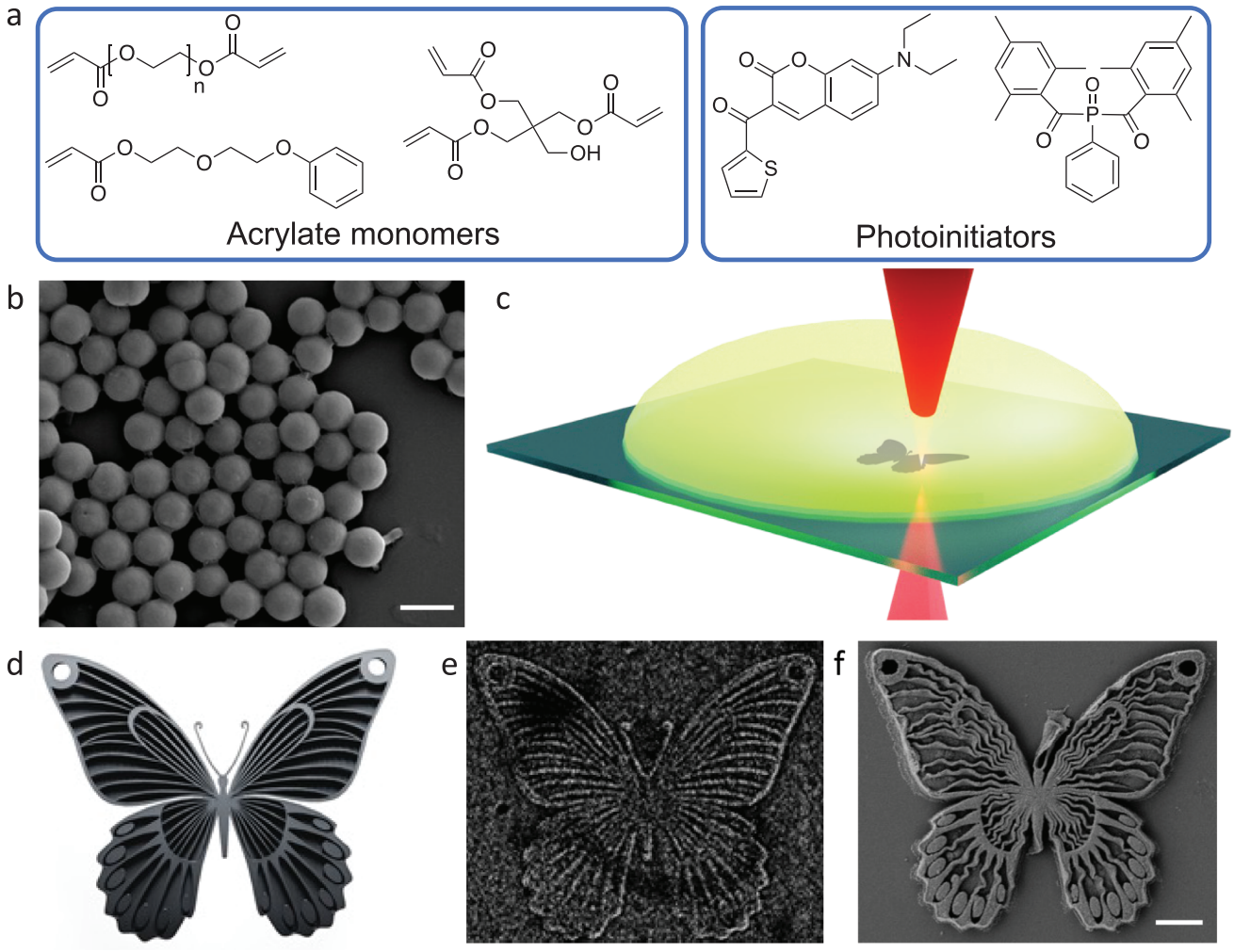

Figure 1. Fabrication of silica nanocomposite microstructures via direct laser writing. a) Photoresist composition showing the acrylate monomers and the choice of photoinitiator; b) SEM image of SiO_2 NP1; c) DLW diagram; d) CAD model of a butterfly structure (150 µm in width and 10 µm in height); e) Image taken during fabrication by DLW using 65% LP (32.5 mW) at 10 000 µm s^{-1} writing speed; f) SEM image of the corresponding butterfly structure post development. The scale bar represents 1 µm in (b) and 20 µm in (f).

by precise engineering of the structural design and modulation of fabrication parameters, a wide gamut of tunable colors across the visible spectrum is achieved. The role of the volume fraction, slicing parameter, and pixel dimension in determining the observed color is elucidated. This added functionality opens up the use of the SiO_2 nanocomposite structures for innovative applications in displays, anti-counterfeiting, and encryption.

2. Results and Discussion

Silica nanoparticles (SiO_2 NP1) were synthesized using the Stöber process (Table S1, Supporting Information). The Stöber process involves the base (ammonia) catalyzed hydrolysis of the silica precursor tetraethyl orthosilicate (TEOS) followed by condensation. It is an attractive synthetic route as it allows sufficient control over the size of the SiO_2 NPs by simply varying the reaction parameters such as temperature, pH, and reactant concentrations.

The average size/ hydrodynamic diameter and the polydispersity index (PDI) of the nanoparticles were obtained via DLS using samples dispersed in deionized water at a concentration of 0.1 wt%, as shown in Figure S1a (Supporting Information). An ammonium hydroxide to TEOS molar ratio of 19:1 gave particles with a hydrodynamic diameter of 785 ± 185 nm (PDI = 0.15) (SiO_2 NP1) (**Figure 1b**). Moreover, SEM analysis of the particles using ImageJ revealed a value of 749 ± 6 nm ($n = 55$) (Figure S1b, Supporting Information).

2.1. 2PP Fabrication of Microstructures Using SiO_2 Nanocomposite Photoresists

A nanocomposite photoresist (Photoresist 1, Table S2, Supporting Information) was prepared using SiO_2 NP1. Poly(ethylene glycol) diacrylate (PEGDA700) was selected as the monomer as it is a biocompatible precursor available at a range of molecular weights, making it suitable for tunable

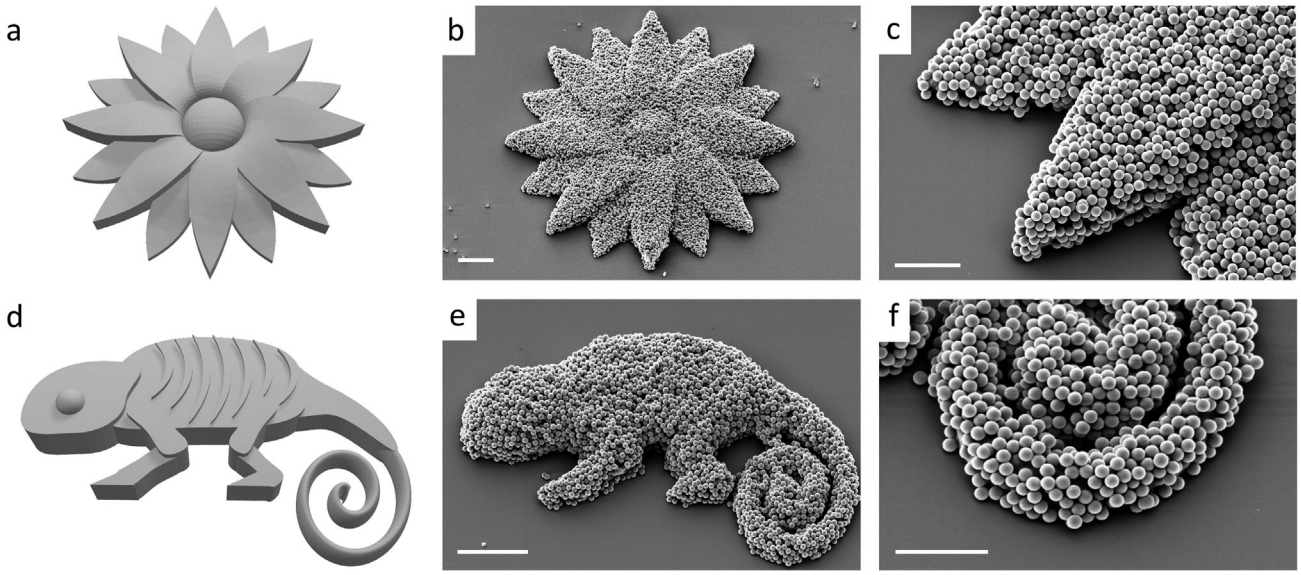

Figure 2. a) Top view of the design used for the fabrication of a daisy-like structure; b, c) SEM of the silica nanocomposite micro-daisy structure and detail, fabricated at 95% LP (47.5 mW) and 10 000 µm s^{-1} using Photoresist 1; d) Top view of the chameleon design; the chameleon structure is 55 µm in width and 5 µm in height; e, f) SEM of the chameleon structure and detail, fabricated at 80% LP (40 mW) and 10 000 µm s^{-1} using Photoresist 1; Scale bar represents 10 µm in (b) and (e), and 5 µm in (c) and (f).

mechanical properties[30,31] Furthermore, its hydrophilicity allows analysis of the swelling behavior of the fabricated structure in aqueous environments.[31b] Moreover, the formation of hydrogen bonding between the silanol groups on the silica surface and the acrylate groups of PEGDA results in the generation of stable dispersions.[30b,32]

33 vol% of SiO_2 NP1 was added to PEGDA700 and a homogenous dispersion was obtained. Next, the ability to fabricate microstructures of PEGDA700 with incorporated SiO_2 NP1 was investigated. Successful fabrication of microstructures is effectively controlled by laser processing parameters such as laser power and scan speed. A daisy-like (**Figure** 2a–c) and a chameleon microstructure (Figure 2d–f) were chosen to identify the optimal laser processing parameters for the fabrication. For these particular designs, high-fidelity, high-resolution structures of SiO_2 NPs nanocomposite were obtained at laser powers ranging from 30 mW (60%) to 50 mW (100%) and a scan speed of 10 000 µm sec^{-1}.

2.2. Mechanical Reinforcement

After confirming that the fabrication of stable microstructures using the SiO_2 NP1-PEGDA700 nanocomposite was possible, the ability of SiO_2 NPs to enhance the mechanical properties of PEGDA 700 structures was studied.

Structures that demonstrate the presence of mechanical reinforcement with ease were designed and fabricated. An ideal structure of choice to visualize the effect of mechanical reinforcement is one that contains a considerable height component and overhangs. These structures require sufficient support to stand upright, and their collapse allows us to qualitatively identify if mechanical reinforcement is taking place. Therefore, blade structures that were 30 µm in height and 150 µm in diameter in which the individual blades function as overhangs were fabricated (**Figure** 3a–c). For comparison, identical structures were fabricated using a control photoresist (Photoresist 2, Table S3, Supporting Information) consisting of only PEGDA700 and the photoinitiator, without any SiO_2 NP1 (Figure 3b). SEM images display a collapse of the overhanging blades in the control structures while SiO_2 NP1 imparts superior structural strength in the nanocomposite structures and prevents the blades from collapsing, under the same experimental conditions (Table S4, Supporting Information). Additionally, bridge structures were chosen to be fabricated due to the ease with which the presence of mechanical reinforcement can be identified by their collapse. A bridge fabricated with a base of 10 × 10 × 20 µm (l × w × h) and a deck of 70 × 10 × 5 µm (l × w × h) (Figure 3d–f) demonstrates the improvement in structural integrity of the fabricated nanocomposite structures compared to a bridge with the same dimensions fabricated with the control photoresist. Moreover, similar mechanical reinforcement could be visualized in the case of other bridge designs (Table S5, Supporting Information) with varying lengths of deck (Bridge 1 = 60 µm, Bridge 2 = 70 µm, Bridge 3 = 80 µm), fabricated at laser powers ranging from LP 60% (30 mW) to LP 100% (50 mW) with a scan speed of 10 000 µm s^{-1}.

Generally, it was established that the collapse of the bridges in which silica nanoparticles were incorporated was suppressed at a lower laser power than the control bridges. Self-supporting structures were obtained in Bridge 1 design at LP 75% (37.5 mW) in photoresist 1, while in photoresist 2, the bridges could only support themselves when LP 80% (40 mW) or higher is utilized. In the case of the Bridge 2 design, self-standing structures were realized at LP 75% (37.5 mW) for photoresist 1 while control structures required a minimum of LP 85% (42.5 mW). Furthermore, Bridge 3 structures typically

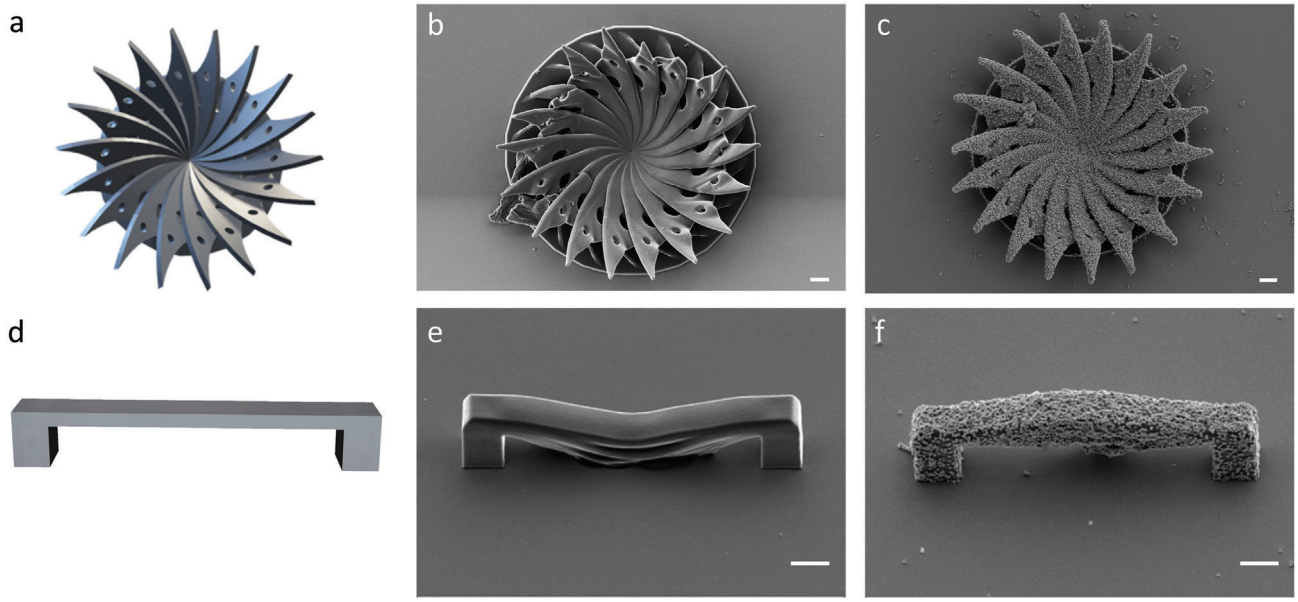

Figure 3. a) Top view of CAD model used for the fabrication of a circular blade structure of 150 µm in diameter and 30 µm in height; b) SEM of the circular blade microstructure fabricated in control Photoresist 2, c) and the silica nanocomposite circular blade structure fabricated using Photoresist 1, where both structures were fabricated at 90% LP (45 mW) and 10 000 µm s^{-1}; d) Top view of CAD design used for the fabrication of bridge structures with bases of 10 × 10 × 20 µm (l × w × h) and a deck of 70 × 10 × 5 µm (l × w × h); e) SEM of a bridge microstructure fabricated in control Photoresist 2, and f) the silica nanocomposite bridge structure fabricated using Photoresist 1, where both structures were fabricated at 80% LP (40 mW) and 10 000 µm s^{-1}; Scale bar represents 10 µm.

showed stable bridges at LP 85% (42.5 mW) in photoresist 1 while control structures required LP 90% (45 mW) to maintain themselves. However, for the longest bridges, with a length of 90 µm, no considerable difference was observed between bridge structures fabricated in photoresist 1 and the control photoresist. In all cases, both the control and the nanocomposite structures were fabricated using identical conditions and laser parameters.

To achieve quantitative data on the mechanical properties, cuboid structures (15 × 15 × 3 µm = l × w × h) were fabricated in Photoresist 1 containing the SiO_2 NP1 and control Photoresist 2 (Figure S2, Supporting Information). Young's modulus of the cuboids was measured in the dry state via AFM. Young's modulus of the control micro-cuboid structures was calculated to be between 104.89 and 148.20 MPa (Figure S2, Supporting Information). These values are in agreement with values obtained for previous work for structures fabricated with PEGDA700 as monomer and of 2,7-bis(2-(4-pentaneoxyphenyl)-vinyl)-anthraquinone as photoinitiator along with 2-benzyl2-(dimethylamino)−4-morpholinobutyrophenone as photosensitizer by Gou et al.[33] A dramatic increase in Young's modulus was observed for the polymer nanocomposite microstructures fabricated with Photoresist 1 with values in the GPa range, spanning from 1.03 to 5.84 GPa (Figure S2, Supporting Information). This is similar to results previously reported in literature obtained by Gojzewski et al.[34] who reported Young's modulus values of 1.233 ± 0.625 GPa for UV polymerized PEGDA/nanosilica composite films with 20 wt% of SiO_2 NPs. This indicates that the mechanical reinforcement demonstrated at the macroscale can be successfully translated to the microscale.

2.3. Structural Color

Above a threshold volume fraction (Equation (1)),at which the solvation layers overlap, interparticle repulsion due to disjoining pressure drives the formation of spontaneous non-close-packed structures that obey the Bragg condition and result in structural coloration.[32,35] By initiating self-assembly of SiO_2 NPs, upon exceeding the threshold volume fraction, ϕ_{th}, followed by entrapment of these assembled SiO_2 NPs in a polymer matrix via DLW-2PP, we can create photonic microstructures. In contrast to mechanical reinforcement studies, the fluorescent photoinitiator DEATC was exchanged for phenylbis(2,4,6-trimethylbenzoyl) phosphine oxide (PBPO) to ensure the observation of structural color. Furthermore, the size of the SiO_2 NPs utilized was reduced to 150 nm (SiO_2 NP2) to obtain interparticle distances (defined as the average distance between the center of two neighboring NPs) in the order of wavelengths in the visible spectrum. Considering a FCC lattice with 4 nanoparticles per unit cell, the volume fraction, ϕ, can be expressed as

$$\phi = \frac{V_{sphere}}{V_{cell}} = \frac{4 \times \frac{4}{3}\pi\left(\frac{d_{SiO_2}}{2}\right)^3}{a^3} = \frac{\pi d_{SiO_2}^3}{3\sqrt{2}D^3} \quad (1)$$

where d_{SiO2} = 150 nm is the average diameter of the non-porous SiO_2 NPs ((SiO_2 NP2), from Sigma Aldrich (see Figure S4, Supporting Information). The threshold volume fraction $\phi_{th} = \frac{\pi d_{SiO_2}^3}{3\sqrt{2}(d_{SiO_2}+73)^3}$ is calculated to be 22.5% in this case.[32] In the general expression, a is the lattice constant of FCC structure and $\frac{\sqrt{2}}{2}a = D$, D represents the center to center distance between two

nearest nanopartices in a FCC (111) plane. According to Equation (1), D can be expressed in terms of the volume fraction, ϕ, such that $D = d_{SiO_2}\left(\frac{3\sqrt{2}\phi}{\pi}\right)^{\frac{-1}{3}}$. Furthermore, in a FCC lattice, D can also be expressed in terms of the separation between layers, for example d_{111} (distance between (111) planes):

$$D = \frac{\sqrt{6}}{2} d_{111} \tag{2}$$

Therefore, d_{111} can be deduced by Equations (1) and (2):

$$d_{111} = \left(\frac{\pi}{3\sqrt{2}\phi}\right)^{\frac{1}{3}} \times \frac{\sqrt{6} d_{SiO_2}}{3} \tag{3}$$

Previous studies have shown that colloidal silica NPs can self-assemble into photonic structures, including in the presence of elastomers to form 3D photonic films.[32] This type of 3D photonic film exhibits a change in structural color by applying stretching, compression, or by changing the ambient temperature. Previous SEM and TEM analyses have shown that face-centered cubic (FCC) crystallization with (111) plane stacking in the z direction is formed during the self-assembly process.[36]

Structural color in reflection with light normally incident on a well-ordered structure can be predicted by the Bragg–Snell law combined with the Maxwell–Garnett approximation below.

$$\lambda_{max} = 2 d_{int} \sqrt{\eta_{eff}^2 - \sin^2 \alpha} \tag{4}$$

where α is the angle of incident light ($\alpha = 0$ in normal reflection), d_{int} is the interlayer spacing and η_{eff} is the effective refractive index. This can be expressed as:

$$\lambda_{\max} = 2 d_{111}\, \eta_{eff} = \left(\frac{\pi}{3\sqrt{2}\phi}\right)^{\frac{1}{3}} \times \frac{2\sqrt{6} d_{SiO_2}}{3} \eta_{eff} \tag{5}$$

where

$$\eta_{eff}^2 = \eta_{polymer}^2 \left[1 - \frac{3\phi\left(\eta_{polymer}^2 - \eta_{silica}^2\right)}{2\eta_{polymer}^2 + \eta_{silica}^2 + \phi\left(\eta_{polymer}^2 - \eta_{silica}^2\right)}\right] \tag{6}$$

d_{111} is the distance between two neighboring FCC (111) planes and ϕ the volume fraction of SiO_2 NP2 as discussed above.[36] For comparison, photoresists of four different volume fractions were formulated (ϕ = 20%, 25%, 33%, 40%) (Tables S6–S9, photoresists 3–6, respectively, Supporting Information).

To determine the effective refractive index, swelling of the polymer was taken into account. Measurement of the swelling was carried out using AFM. Samples using Photoresist 5 (based on PEGDA700) revealed a percentage increase in height after swelling of ≈7% in IPA, 10% in EtOH, and 25% in DI water (Figure S3, Supporting Information). This percentage increase in swelling showed only small fluctuations across the range of laser powers and slicing distances employed in this study (Figures S3 and S4, Supporting Information). η_{eff} is the effective refractive index of polymer expanding 7% and incorporating ϕ volume fraction of SiO_2 NP2, η_{silica} is the refractive index of the silica nanoparticles (1.45),[32] $\eta_{polymer}$ is the refractive index of the polymers PEG-PEA (1.502),[32] and PEGDA (1.51).[37] The calculated effective refractive indices for the SiO_2 NP2 in polymer using Equation (6), with or without expansion, are listed in Table S11 (Supporting Information). For the expanded case the increased values of d_{111} are used to determine the volume fraction of SiO_2 NP2 in the expanded polymer and the corresponding η_{eff} is calculated using Equation (6). A decrease in the η_{eff} can be observed with increasing volume fraction of silica NPs. d_{111} for ideal FCC (111) structures with ϕ = 20, 25, 33, and 40% are listed in Table S12 (Supporting Information), showing a decrease with increasing silica NP volume concentration. The reflection peaks calculated according to Equation (3) are also shown in Table S12 (Supporting Information). A clear blueshift of the calculated reflection peak can be seen with increasing silica NP volume fraction. Structures for which ϕ = 20%, 25%, 33%, and 40% were fabricated and characterized using SEM and optical microscopy.

The SEM analysis of microfabricated cuboid structures cleaved from the glass substrate indicates the absence of long-range order (Figure S4, Supporting information). The disruption of long-range order can be attributed to the polydispersity of the SiO_2 NP2. It has been previously confirmed that the presence of polydisperse nanoparticles in a polymer matrix results in the formation of a quasi-ordered arrangement containing short-range order but lacking long-range order.[23,36,38] Even though crystallization is suppressed due to polydispersity of SiO_2 NP2 in the photoresist, interparticle repulsion between the SiO_2 NP2 creates short-range ordering and therefore, the structure is not simply amorphous, but quasi-ordered. The arrangement is influenced by two parameters, namely size contrast and mixing ratio.[39] DLS measurements, resulting in a PDI of 0.089, and SEM images are indicative of this polydispersity present in the SiO_2 NP2 sample utilized for the preparation of photonic microstructures (Figures S5 and S6, Supporting information). It has been previously reported that a PDI below 0.05 results in the formation of periodic structures, whilst quasi-amorphous structures are formed when the PDI of the nanoparticles is above 0.05.[23] Therefore, the structural color in these microfabricated structures containing quasi-ordered SiO_2 NP2 likely results from a combination of Bragg diffraction of visible light resulting in the production of a photonic band gap (PBG) arising from regions in which the SiO_2 NP2 are ordered and Mie scattering emerging from regions in which the SiO_2 NP2 are present in a disordered manner.[38] A periodic variation in the refractive index results in the formation of a PBG in the ordered regions. Jin et al.[40] demonstrated, using multiple-scattering theory, that a PBG exists in quasi-ordered structures. The presence of short-range order results in the formation of the first band gap while long-range order is necessary for the creation of higher band gaps.

Darkfield scattering is used to measure the optical properties of the structures and to reveal the structural colors that are weaker than the surface reflectance in brightfield mode. In air, the brightfield reflectance spectra are dominated by the interface reflection and the darkfield by the edge scattering, with typical examples shown in Figure S7 (Supporting Information). Microstructures of dimensions 10 µm × 10 µm × 60 µm (l × w × h) were fabricated at all four volume fractions (**Figure** 4a). The effect of SiO_2 NP concentration on the structural color was investigated, as shown in

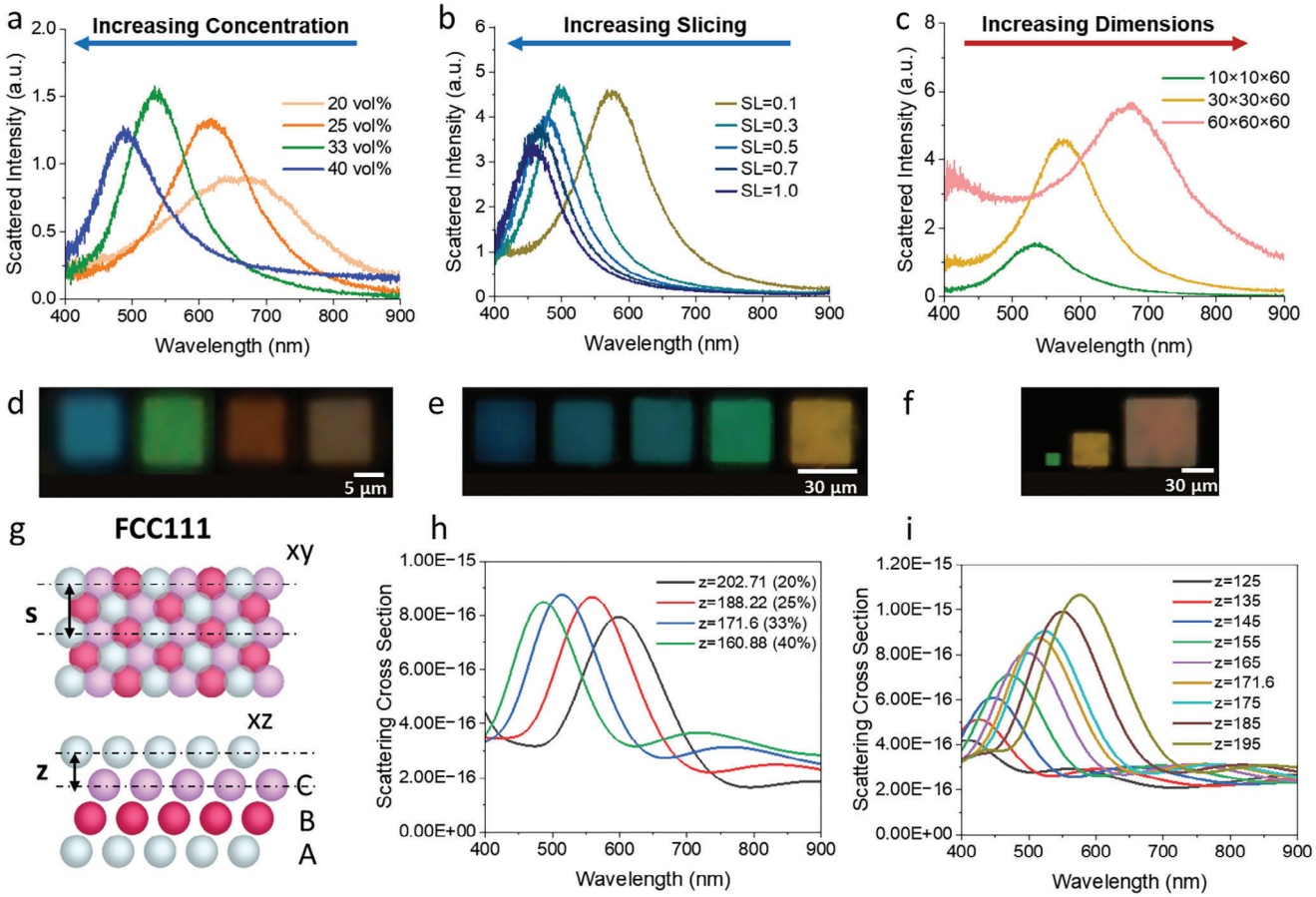

Figure 4. Darkfield scattering spectra obtained from cuboid samples immersed in IPA fabricated with variation in a) SiO_2 NP2 concentration(while LP and SL are kept constant at LP = 45 mW, SL = 0.1 μm), b) slicing distance (μm)(while LP and SiO_2 NP2 concentration is kept constant at LP = 45 mW and SiO_2 NP2 at 33 vol%) and c) *XY* dimensions (while LP and SL were kept constant at LP = 45 mW, SL = 0.1 μm and SiO_2 NP2 at 33 vol%). d-f) the corresponding dark field optical microscopy images. All images and experimental spectra were taken using a 20X objective (NA = 0.4). g) Schematic diagram shows the FCC (111) crystalline structure. FDTD simulation results of scattering cross-section of FCC (111) in h) different silica NP concentrations (20, 25, 33, and 40 vol%) and i) different (111) plane distance *z*. The design dimensions of the cuboid microstructures are d) 10 μm × 10 μm × 60 μm; e) 30 μm × 30 μm × 60 μm; f) 10 μm × 10 μm × 60 μm, 30 μm × 30 μm × 60 μm and 60 μm × 60 μm × 60 μm (left to right).

Figure 4. As the SiO_2 NP concentration increases there is a clear blue shift of the peak of the darkfield scattering spectrum. Peak wavelengths of 666, 618, 533, and 486 nm were obtained for ϕ = 20, 25, 33, and 40%, respectively, with a total shift of 180 nm from ϕ = 20% to 40%.

A comparison of the experimental peak wavelengths with those expected from Equation (5) is given in Table S12 (Supporting Information). The blue shift with increasing SiO_2 NP concentrations in Figure 4a shows the same trend as predicted from the Bragg–Snell's description, and arises due to the decreasing distances between neighboring particles and FCC (111) planes. However, it must be noted that the Bragg–Snell description is for reflection under normal incident light. In this work, the measurements have been taken in darkfield mode with an objective of NA = 0.4, unless otherwise specified. To explore further the origin of the observed color and assumption of an FCC (111) structure, the scattering from an ideal—FCC (111) non-closed-packed structure (Figure 4g) was numerically calculated using a commercial finite difference time domain simulation (FDTD) tool, Lumerical. Further details are provided in Figure S8a (Supporting Information) and a scattering spectrum for a single SiO_2 NP in the hydrogel host medium is also shown in Figure S8b (Supporting Information) for reference. Figure 4h shows the scattering cross-section spectra for the different SiO_2 NP concentrations. The trends of the experimental spectra are well reproduced by the numerically simulated spectra, and the peak wavelengths are given in Table S12 (Supporting Information). The discrepancy between the peak wavelengths from the experimental spectra and the simulated scattering spectra decreases with increasing volume fraction and they are in agreement at the highest volume fraction. This can be attributed to a higher level of order in the case of a high SiO_2 NP concentration, which is closest to the perfect FCC structure of the simulation. The lowest volume fraction investigated, ϕ = 20%, is below the threshold volume fraction and shows the largest discrepancy and the broadest spectrum.

The process of DLW-2PP, where structures are fabricated in a voxel-by-voxel manner, allows for control over the spacing between the layers in the z direction commonly referred to as the slicing distance (SL). This in turn allows for the precise variation of the interparticle distance in the z direction. For this

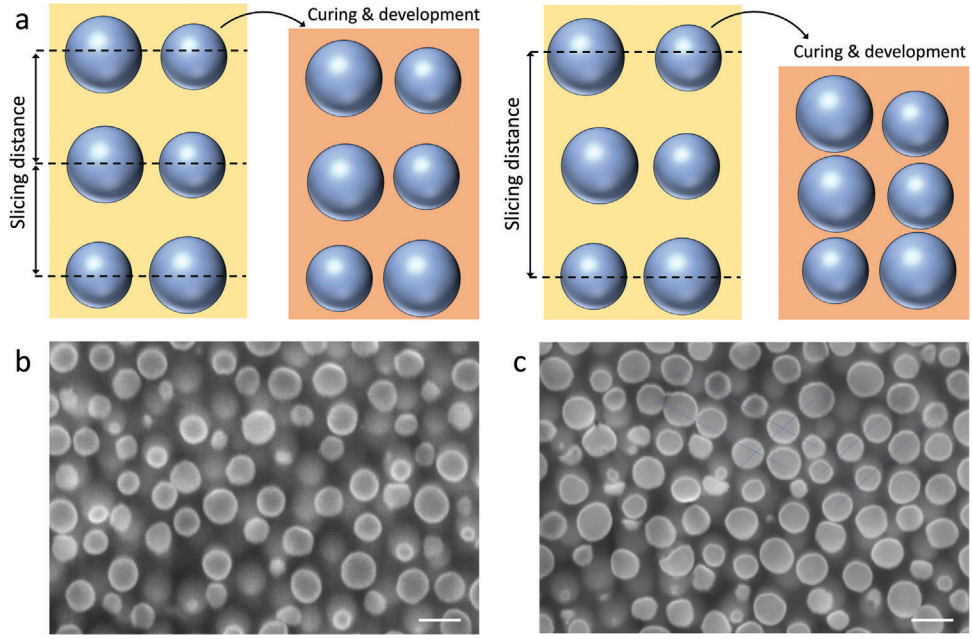

Figure 5. The control of slicing distance in DLW allows for fine-tuning of the resulting z distance between neighboring particles, and therefore the optical properties of the resulting microstructures. a) Diagram showing that large slicing distance results in increased collapse of the nanoparticles and therefore a smaller z interparticle distance post-development; In contrary, a small slicing distance (comparable to the nanoparticle size) locks the material in place during polymerization and only small particle collapse can occur. FIB slice of microstructures post development fabricated using b) 0.1 µm and c) 1 µm slicing distance, respectively. The scale bar represents 200 nm. Yellow denotes the unpolymerized photoresist, while orange denotes the polymer network after polymerization and development.

purpose, microstructures were fabricated with dimensions of 30 µm × 30 µm × 60 µm (l × w × h) (Figure 4b) with z slicing distance of 0.1, 0.3, 0.5, 0.7, and 1 µm. Using this approach, all colors spanning the visible region were obtained, and a blue shift was observed as the slicing distance was increased. Peak wavelengths of 568, 497, 479, 472, and 452 nm were obtained for a slicing distance of 0.1, 0.3, 0.5, 0.7, and 1 µm, respectively, with a total shift of 116 nm when the slicing distance was increased from 0.1 µm to 1 µm (Figure 4b). Ordinarily, a red shift might be predicted, where the increase in slicing distance might be expected to produce a larger interplanar distance in the z direction, as described by Equation (2) and shown in Figure 4i. However, during the development process, solvent washing for the removal of the unpolymerized resin causes a collapse of the layers within the structure (**Figure 5**). A bigger collapse was experienced by structures with a larger slicing distance resulting in a smaller interlayer distance in the z direction, as a larger volume of unpolymerized material was present between the layers and removed during development (Figure 5a). This has been previously observed in the case of 2PP fabricated microstructures containing cholesteric reactive mesogens, where controlling the extent of structural shrinkage that occurred during development was utilized to vary the effective pitch and thus tune the photonic band gap.[36] When a large slicing distance was used, this caused a large fraction of unpolymerized material to be removed, resulting in enhanced shrinkage of the structure. To further prove this phenomenon in the case of the silica nanocomposite structures presented herein, focused ion beam (FIB) sectioning was used for microstructures fabricated using different slicing distances of 0.1 µm and 1 µm, respectively. As can be seen from Figure 5b,c, a larger slicing distance does result in a microstructure with a considerably smaller interparticle z distance, which in turn translates into a blue shift of the color with increasing slicing distance. These trends are confirmed by the FDTD simulation scattering spectra, shown in Figure 4i, which show the blue shift and spectral narrowing of the scattering peak as the interparticle separation is reduced.

Finally, the relative contributions from the quasi-ordering compared with the random scattering in different directions within the structures were modulated by varying the dimensions of the structures. For this purpose, the height of the structures was maintained constant at 60 µm while the x and y dimensions of the cuboid structures were varied ($x = y$ = 10, 30, 60, and 90 µm, respectively). A red spectral shift was observed as the x and y dimensions were increased as shown in Figure 4c. Peak wavelengths of 533, 569, and 676 nm were obtained for cubes of 10 µm × 10 µm × 60 µm, 30 µm × 30 µm × 60 µm, and 60 µm × 60 µm × 60 µm (x × y × z), respectively, with a total shift of 143 nm between the smallest and largest structures used in this study. A saturation is reached at x and y dimensions of 60 µm and irrespective of the size, the structural color remains red. This is explored further using the FDTD numerical calculations of the scattering cross-section spectra from the side of the cubes compared with the top of the cube, shown in Figure S9 (Supporting Information). The spectra taken from the side of the cube are very broad with a peak in the blue, whereas the scattering from the top is red-shifted and narrower as expected for Bragg diffraction. Therefore, when the scattering from the four sides of the cube dominates the total collected scattered light, the observed color is dominated by bluer components. The light from the top surface

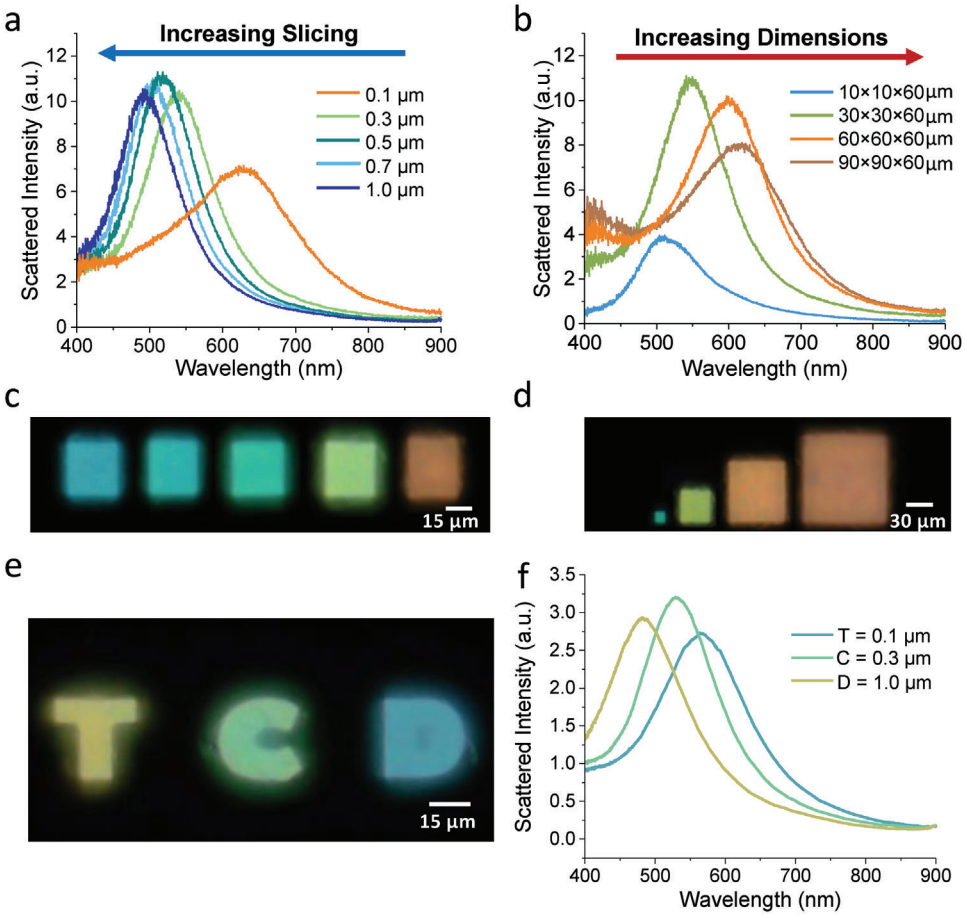

Figure 6. Darkfield scattering spectra obtained from cuboid samples immersed in IPA fabricated with variation in a) slicing distance (LP: 30 mW, SiO_2 NP2 at 33 vol%) and b) *XY* dimensions (LP: 30 mW, SL: 0.3S, SiO_2 NP2 at 33 vol%), the corresponding dark field optical microscopy images c, d). The design dimensions of the cuboid microstructures are c) 30 × 30 × 60 µm; d) 10 × 10 × 60, 30 × 30 × 60, 60 × 60 × 60, and 90 × 90 × 60 µm (left to right). e) Dark field optical microscopy image showing the TCD structure fabricated using different slicing distances; Letter T has 0.1 µm slicing, C has 0.3 µm slicing and D has 1 µm slicing; The corresponding dark-field scattering spectra are shown in (f). All of the images and spectra were taken with 20× objective (NA = 0.4).

makes a larger contribution to the collected scattered light as the *x* and *y* dimensions are increased.

Further structural color analysis was carried out by replacing PEGDA700 with PEGPEA (Table S10, Photoresist 7, Supporting Information). The "TCD" pattern based on the PEGPEA photoresist is shown in **Figure 6**, with the corresponding experimental scattering spectra. The same dependencies on the slicing and structure dimensions are observed, and it is shown how these can be exploited to print color patterns using cuboids of varying dimensions. The scattered colors appear more brilliant using the PEGPEA photoresist which may indicate a higher level of quasi-order. This could be attributed to the dense solvation layer formed upon hydrogen bonding with the surface hydroxyl groups, which has been shown to result in efficient self-assembly.[41]

3. Conclusion

We have successfully fabricated 3D microstructures using acrylate-based photoresists incorporating silica nanoparticles at a range of concentrations using two-photon lithography. First, silica nanoparticles (SiO_2 NP1) were proven to successfully mechanically reinforce the microstructures compared to the neat photoresist under the same experimental conditions. This reinforced material has potential applications in multimaterial fabrication for soft actuators where it can be utilized to form rigid regions to support softer materials.

Furthermore, the presence of silica nanoparticles (SiO_2 NP2) above a threshold concentration imparted structural coloration to the fabricated microstructures. By precise engineering of the structural design and modulation of fabrication parameters, a wide gamut of tunable colors from the blue to the red spectral regions was achieved. Moreover, the underlying mechanism for color generation and its dependence on the volume fraction, slicing, and pixel dimensions has been explained. A full understanding of color generation opens a route to innovative applications in displays, anti-counterfeiting, and encryption.

4. Experimental Section

Materials and Photoresist Preparation: Silica nanoparticles (SiO_2 NP2, non-porous, 150 nm), poly(ethylene glycol) diacrylate (PEGDA $M_n \cong$ 700 g mol^{-1}), poly(ethylene glycol) phenyl ether acrylate (PEGPEA $M_n \cong$

324 g mol^{-1}), pentaerythritol triacrylate, tween 80, ammonium hydroxide (28–30%, ACS grade), tetraethyl orthosilicate (98%, reagent grade) and 3-(trimethoxysilyl) propyl methacrylate were obtained from Sigma–Aldrich, Ireland, and used as received. Phenylbis(2,4,6-trimethylbenzoyl) phosphine oxide (PBPO) was obtained from TCI, Japan. 7-Diethylamino-3-thenoylcoumarin (DEATC) was obtained from Alphachemical, USA. All solvents used, including methanol, ethanol, acetone, isopropyl alcohol (IPA), and propylene glycol methyl ether acetate (PGMEA) were high-performance liquid chromatography grade (HPLC) purchased in anhydrous form, from Sigma–Aldrich and used without further purification.

SiO_2 NP1 (d = 720 ± 60 nm) was synthesized via the Stöber process. In a round-bottomed flask, ethanol (50 mL) and ammonium hydroxide (10 mL) were heated to 25 °C with magnetic stirring at 150 rpm for 15 min. A solution of TEOS (3 mL) in ethanol (10 mL) was added dropwise to the stirring ammonium hydroxide/ethanol solution using a syringe pump at a rate of 1 mL min^{-1}. The solution was left to react at 25 °C for 24 h. A visible color change from transparent to milky white was observed. The nanoparticles were isolated through repeated centrifuging (universal 320 Hettich Zentrifugen), 12 000 rpm for 15 min. They were washed with deionized water, isolated via further centrifuging at 12 000 rpm for 15 min, and dried in the oven (60 °C, 2 h).

Photoresist Preparation: Silica nanocomposite photoresists using two different size SiO_2 NP were prepared. SiO_2 NP1 33 vol% to PEGDA (Table S2) and SiO_2 NP2 (20, 25, 33 and 40 vol% to PEGDA, as detailed in Tables S6–S9). PBPO (1.94 mol% to PEGDA) or DEATC (1.05 mol% to PEGDA) were used as photoinitiators. Furthermore, the PEGDA monomer was replaced by PEGPEA to which SiO_2 NP2 (33 vol% to PEGPEA, Table S11, Supporting Information) pentaerithritol triacrylate (32.5 mol% to PEGPEA) and PBPO (3.55 mol%) were added.

Direct laser writing: 3D microstructures were fabricated via two-photon polymerization using the commercial lithography system, Nanoscribe GT Photonic Professional system (Nanoscribe GmbH), operating at 780 nm. All structures were fabricated on high-precision glass substrates (No 1.5H of 170 ± 5 µm thickness, Thermo-Fisher) in the oil immersion configuration using a 63× immersion objective (Zeiss, Plan Apochromat). Prior to fabrication, the glass substrates were washed with the following solvents in order of increasing polarity, acetone, IPA, ethanol, methanol, and deionized water. The slides were dried with N_2 and placed in a UV Ozone cleaner (Osssila, United Kingdom) for 20 min followed by immersion in a solution containing 3 vol% 3-(trimethoxysilyl) propyl methacrylate, and 0.1 vol% acetic acid in ethanol. The slides were then dried in the oven. A drop of the unpolymerized photoresist was placed in the center of the glass coverslip, while a drop of oil (Zeiss Immersol 518F) was placed in the center of the glass substrate on the opposite side. The structure stl. file was imported into DeScribe 2.4.4 software. After fabrication, the unpolymerized resist was removed by rinsing the slide with PGMEA, followed by a mixture of 5 wt% tween 80 in ethanol and IPA. All solvents were heated to 60 °C.

3D design: Several of the 3D structures used in this work were designed using Blender software and adapted as needed in DeScribe software. These include the bridge structures (10 × 10 × 20 µm (l × w × h) and a deck of 10 × 5 µm (w × h) with lengths of 60 µm (bridge 1), 70 µm (bridge 2), 80 µm (bridge 3) and 90 µm (bridge 4)); and arrays of cubes (10 × 10 × 60, 30 × 30 × 60, 60 × 60 × 60, and 90 × 90 × 60 µm ($x \times y \times z$)).The butterfly, blades, chameleon, and TCD letter structures were adapted from files licensed under the Attribution-NonCommercial 4.0 International (CC BY-NC 4.0 DEED) license and available for download under the links below

Blades: https://www.thingiverse.com/thing:2757443
Butterfly: https://www.thingiverse.com/thing:816098
TCD letters: https://www.thingiverse.com/thing:299169

SEM Imaging and Analysis: Scanning electron microscopy of 2PP-fabricated microstructures was carried out using a Zeiss ULTRA plus scanning electron microscope. An accelerating voltage of 5 kV was used under the SE2 mode to acquire all images. Prior to SEM imaging, the structures were coated with a 10 nm Au/Pd layer using a Cressington sputter coater 208HR. A 57 × 0.1 mm Au/Pd target (TED PELLA INC.) was used to coat the structures under an inert atmosphere of argon for 15 s. The SiO_2 NP1s particle diameter was measured from top–down SEM images using the particle analysis function on ImageJ. A minimum of 26 diameter measurements were obtained per SiO_2 NP1s synthesis to ensure a representative sample of the particles.

Dynamic Light Scattering (DLS) Analysis: DLS measurements were performed on Malvern Zetasizer Nano ZS, using a 633 nm HeNe laser. Samples were prepared by dispersing SiO_2 NP1 in deionized water (0.01 wt%). Samples were tested in quartz cuvettes with a path length of 1 cm. The machine was operated in a backscatter mode at an angle of 173°. Samples were equilibrated for 120 s at 25 °C prior to measurement. Parameters at 25 °C of media refractive index $n = 1.334$, media viscosity of 0.890 cP, and sample refractive index $n = 1.45$[32] were assumed in the measurement.

AFM Imaging and Analysis: Atomic force microscopy (AFM) both in air and liquid medium was performed using MFP-3D (Asylum Research). In liquid mediums such as IPA, ethanol, and Milli-Q water, measurements were performed using a fluid cell setup from Asylum systems. In this, the cell was filled with 1 mL of the respective solvent. The topography measurements were done using an AFM probe (Electrical all-in-one, BudgetSensors, Bulgaria) with four different platinum-coated AFM cantilevers on a single AFM holder chip in which cantilever D with tip radius <25 nm, resonant frequency of ≈350 kHz, and a spring constant of 40 N m^{-1} was used. AFM images were obtained using contact mode with 256 lines per scan direction and with a scan rate of 0.4 Hz and scan angle of 90°. The AFM height images were processed using Gwyddion AFM software (version 2.6).

FIB Imaging and Analysis: The samples were mounted on a stub with carbon tape. The samples were Au/Pd coated prior to milling. FIB-SEM (Zeiss AURIGA) was conducted at a tilt angle of 54° using a 5 mm working distance (eucentric point). FIB milling was performed at 30 kV and 240 pA. Subsequently, SEM images of the cross-sections were collected using a 30 µm aperture and an accelerating voltage of 5 kV.

Darkfield Measurements: The 20× objective lens (NA = 0.4, Olympus LMPlan FL N) combined with ane Olympus BX53 microscope was used to take the darkfield measurements. The images and spectra were taken using a CCD camera and an Andor 230i spectrometer, respectively. The normalized scattering spectra were obtained using $(SS_{sample} - SS_{bg})/(SS_{diffuser} - SS_{bg})$ where SS_{sample} is the scattering spectrum measured from the sample, SS_{bg} is the background spectrum from the ambient environment and $SS_{diffuser}$ is the reference spectrum measured using a glass cell filled with solvents placed on a ceramic diffuser.

Numerical Simulations: The Lumerical software, FDTD solver (finite difference time domain) was used to calculate the cross-section scattering of the 3D photonic crystals. The model FCC lattice of silica nanoparticles with (111) plane in the z direction was built as shown in Figure S8 (Supporting Information). The commercial silica nanoparticles (refractive index of "SiO_2 (Glass) – Palk" in refractive index database in FDTD) with a diameter of 150 nm were used in the models. The TFSF source surrounded the lattice structure. Six monitors were placed outside the light source to capture the signal. The total power signal from five monitors (except the one in the transmission position) was divided by light intensity to normalize the scattering of the cross-section. The refractive index of PEGPEA (1.502)[32] and PEGDA (1.51),[37] as well as the refractive index of isopropanol (1.3772),[42] were used to calculate the ambient effective refractive index according to Maxwell–Garnett approximation. The structure model was meshed with 5 nm resolution in three directions. PML boundary conditions were set in the *x*, *y*, and *z* directions.

Supporting Information

Supporting Information is available from the Wiley Online Library or from the author.

Acknowledgements

A.A. and J.Q. contributed equally to this work. This research received funding from the European Research Council (ERC) Starting Grant (No.

802929 – ChemLife), Science Foundation Ireland (SFI), and European Regional Development Fund (ERDF) under grant number 12/RC/2278_P2. J.Q. acknowledges funding from the Chinese Scholarship Council. A.L.B. acknowledges SFI awards 16/IA/4550 and 17/RC-PhD/348. C.D. acknowledges support from the European Union (ERC, Grant No. 101077430 – BIO4D). S.K. and L.F. acknowledge funding from the European Horizon 2020 Research and Innovation Programme (No. 899349 – 5D NanoPrinting). T.F. acknowledges support from the Irish Research Council, Government of Ireland Postgraduate Scholarship GOIPG/2022/944. The DLW-2PP fabrication and the imaging for this project were carried out at the Additive Research Laboratory (AR-Lab) and the Advanced Microscopy Laboratory (AML), Trinity College Dublin, Ireland. The AR-Lab and AML are SFI-supported centers, part of the CRANN Institute, and affiliated with the AMBER Centre.

Open access funding provided by IReL.

Conflict of Interest

The authors declare no conflict of interest.

Data Availability Statement

The data that support the findings of this study are available in the supplementary material of this article.

Keywords

direct laser writing, nanocomposites, photonics, silica nanoparticles, two-photon polymerization

Received: November 4, 2023
Revised: February 5, 2024
Published online: March 5, 2024

[1] K.-S. Lee, R. H. Kim, D.-Y. Yang, S. H. Park, *Prog. Polym. Sci.* **2008**, *33*, 631.
[2] J. J. Sandford O'Neill, PhD diss., University of Oxford, **2021**.
[3] R. K. Jayne, T. J. Stark, J. B. Reeves, D. J. Bishop, A. E. White, *Adv. Mater. Technol.* **2018**, *3*, 1700293.
[4] a) K. Sugioka, J. Xu, D. Wu, Y. Hanada, Z. Wang, Y. Cheng, K. Midorikawa, *Lab Chip* **2014**, *14*, 3447; b) F. Mayer, S. Richter, J. Westhauser, E. Blasco, C. Barner-Kowollik, M. Wegener, *Sci. Adv.* **2019**, *5*, eaau9160.
[5] Y. Liu, H. Wang, J. Ho, R. C. Ng, R. J. Ng, V. H. Hall-Chen, E. H. Koay, Z. Dong, H. Liu, C.-W. Qiu, *Nat. Commun.* **2019**, *10*, 4340.
[6] a) O. Dadras-Toussi, V. Raghunathan, S. Majd, M. R. Abidian, presented at *44th Annual Int. Conf. of the IEEE Engineering in Medicine & Biology Society (EMBC)*, Glasgow, Scotland, UK, July, **2022**; b) O. Dadras-Toussi, M. Khorrami, M. R. Abidian, presented at *43rd Annual Int. Conf. of the IEEE Engineering in Medicine & Biology Society (EMBC)*, Mexico, October, **2021**.
[7] U. Bozuyuk, O. Yasa, I. C. Yasa, H. Ceylan, S. Kizilel, M. Sitti, *ACS Nano* **2018**, *12*, 9617.
[8] Z.-C. Ma, Y.-L. Zhang, B. Han, X.-Y. Hu, C.-H. Li, Q.-D. Chen, H.-B. Sun, *Nat. Commun.* **2020**, *11*, 4536.
[9] W. Xiong, Y. Liu, L. J. Jiang, Y. S. Zhou, D. W. Li, L. Jiang, J. F. Silvain, Y. F. Lu, *Adv. Mater.* **2016**, *28*, 2002.
[10] a) U. Staudinger, G. Zyla, B. Krause, A. Janke, D. Fischer, C. Esen, B. Voit, A. Ostendorf, *Microelectron. Eng.* **2017**, *179*, 48; b) K. Masui, S. Shoji, K. Asaba, T. C. Rodgers, F. Jin, X.-M. Duan, S. Kawata, *Opt. Express* **2011**, *19*, 22786.
[11] a) Z. Xiong, C. Zheng, F. Jin, R. Wei, Y. Zhao, X. Gao, Y. Xia, X. Dong, M. Zheng, X. Duan, *Sens. Actuators, B* **2018**, *274*, 541; b) H. Ceylan, I. C. Yasa, O. Yasa, A. F. Tabak, J. Giltinan, M. Sitti, *ACS Nano* **2019**, *13*, 3353.
[12] A. Marino, J. Barsotti, G. De Vito, C. Filippeschi, B. Mazzolai, V. Piazza, M. Labardi, V. Mattoli, G. Ciofani, *ACS Appl. Mater. Interfaces* **2015**, *7*, 25574.
[13] a) R. D. Fonseca, D. S. Correa, E. C. Paris, V. Tribuzi, A. Dev, T. Voss, P. H. B. Aoki, C. J. L. Constantino, C. R. Mendonca, *J. Polym. Sci. B Polym. Phys.* **2014**, *52*, 333; b) Y. Peng, S. Jradi, X. Yang, M. Dupont, F. Hamie, X. Q. Dinh, X. W. Sun, T. Xu, R. Bachelot, *Adv. Mater. Technol.* **2019**, *4*, 1800522.
[14] A. Groetsch, S. Stelzl, Y. Nagel, T. Kochetkova, N. C. Scherrer, A. Ovsianikov, J. Michler, L. Pethö, G. Siqueira, G. Nyström, *Small* **2023**, *19*, 2202470.
[15] O. Dadras-Toussi, M. Khorrami, A. S. C. Louis Sam Titus, S. Majd, C. Mohan, M. R. Abidian, *Adv. Mater.* **2022**, *34*, 2200512.
[16] Q. Guo, R. Ghadiri, T. Weigel, A. Aumann, E. L. Gurevich, C. Esen, O. Medenbach, W. Cheng, B. Chichkov, A. Ostendorf, *Polymers* **2014**, *6*, 2037.
[17] K. Liu, H. Ding, S. Li, Y. Niu, Y. Zeng, J. Zhang, X. Du, Z. Gu, *Nat. Commun.* **2022**, *13*, 4563.
[18] J. Sun, B. Bhushan, J. Tong, *RSC Adv.* **2013**, *3*, 14862.
[19] J. Liao, C. Ye, J. Guo, C. E. Garciamendez-Mijares, P. Agrawal, X. Kuang, J. O. Japo, Z. Wang, X. Mu, W. Li, *Mater. Today* **2022**, *56*, 29.
[20] J. Hou, H. Zhang, Q. Yang, M. Li, Y. Song, L. Jiang, *Angew. Chem., Int. Ed.* **2014**, *53*, 5791.
[21] J. Wei, X. Aeby, G. Nyström, *Adv. Mater. Technol.* **2023**, *8*, 2200897.
[22] L. Bai, Z. Xie, W. Wang, C. Yuan, Y. Zhao, Z. Mu, Q. Zhong, Z. Gu, *ACS Nano* **2014**, *8*, 11094.
[23] C.-F. Lai, Y.-C. Wang, H.-C. Hsu, *J. Mater. Chem. C* **2016**, *4*, 398.
[24] M. Arjmandi, M. Ramezani, *J. Mech. Behav. Biomed. Mater.* **2019**, *95*, 196.
[25] J. Zaragoza, N. Babhadiashar, V. O'Brien, A. Chang, M. Blanco, A. Zabalegui, H. Lee, P. Asuri, *PLoS One* **2015**, *10*, e0136293.
[26] Z. Luo, R. Hong, H. Xie, W. Feng, *Powder Technol.* **2012**, *218*, 23.
[27] T. Doualle, J.-C. André, L. Gallais, *Opt. Lett.* **2021**, *46*, 364.
[28] F. Kotz-Helmer, A. S. Quick, P. Risch, T. Martin, T. Hoose, M. Thiel, D. Helmer, B. E. Rapp, *Adv. Mater.* **2021**, *33*, 2006341.
[29] X. Wen, B. Zhang, W. Wang, F. Ye, S. Yue, H. Guo, G. Gao, Y. Zhao, Q. Fang, C. Nguyen, *Nat. Mater.* **2021**, *20*, 1506.
[30] a) X. Dai, X. Chen, L. Yang, S. Foster, A. J. Coury, T. H. Jozefiak, *Acta Biomater.* **2011**, *7*, 1965; b) A. Hocken, Y. Yang, F. L. Beyer, B. F. Morgan, K. Kline, T. Piper, M. D. Green, *Ind. Eng. Chem. Res.* **2019**, *58*, 14775; c) J. E. Koskela, S. Turunen, L. Ylä-Outinen, S. Narkilahti, M. Kellomäki, *Polym. Adv. Technol.* **2012**, *23*, 992.
[31] a) S. F. Klimaschewski, J. Küpperbusch, A. Kunze, M. Vehse, *J. Mech. Energy Eng.* **2022**, *6*, 33; b) H. Zhang, L. Wang, L. Song, G. Niu, H. Cao, G. Wang, H. Yang, S. Zhu, *J. Appl. Polym. Sci.* **2011**, *121*, 531.
[32] G. H. Lee, T. M. Choi, B. Kim, S. H. Han, J. M. Lee, S.-H. Kim, *ACS Nano* **2017**, *11*, 11350.
[33] X. Gou, M. Zheng, Y. Zhao, X. Dong, F. Jin, J. Xing, X. Duan, *Appl. Surf. Sci.* **2017**, *416*, 273.
[34] H. Gojzewski, M. Sadej, E. Andrzejewska, M. Kokowska, *Eur. Polym. J.* **2017**, *88*, 205.
[35] L. D. C. de Castro, O. N. Oliveira Jr, *ACS Appl. Nano Mater.* **2022**, *5*, 2906.
[36] G. H. Lee, S. H. Han, J. B. Kim, J. H. Kim, J. M. Lee, S.-H. Kim, *Chem. Mater.* **2019**, *31*, 8154.
[37] H. Takahashi, T. Kan, G. Lee, N. Dönmez, J. Kim, J. Park, D. Kim, Y. J. Heo, *Appl. Phys. Express* **2020**, *13*, 076503.
[38] K. Ueno, A. Inaba, Y. Sano, M. Kondoh, M. Watanabe, *Chem. Commun.* **2009**, *24*, 3603.

[39] G. H. Lee, J. B. Kim, T. M. Choi, J. M. Lee, S. H. Kim, *Small* **2019**, *15*, 1804548.
[40] C. Jin, X. Meng, B. Cheng, Z. Li, D. Zhang, *Phys. Rev. B* **2001**, *63*, 195107.
[41] S. R. Raghavan, H. J. Walls, S. A. Khan, *Langmuir* **2000**, *16*, 7920.
[42] J. Qian, S. Kolagatla, A. Pacalovas, X. Zhang, L. Florea, A. L. Bradley, C. Delaney, *Adv. Funct. Mater.* **2023**, *33*, 2211735.

